THE JOURNAL OF
PHYSICAL CHEMISTRY C

Article

Cite This: *J. Phys. Chem. C* 2019, 123, 12321−12334

pubs.acs.org/JPCC

Defect Chemistry of Er^{3+}-Doped TiO_2 and Its Photocatalytic Activity for the Degradation of Flowing Gas-Phase VOCs

Zepeng Rao,[†,‡] Xiaofeng Xie,[*,†] Xiao Wang,[†] Asad Mahmood,[†] Shengrui Tong,[§] Maofa Ge,[§] and Jing Sun[*,†]

[†]Shanghai Institute of Ceramics, Chinese Academy of Sciences, 1295 Dingxi Road, Shanghai 200050, China
[‡]University of Chinese Academy of Sciences, 19 (A) Yuquan Road, Beijing 100049, China
[§]Institute of Chemistry, Chinese Academy of Sciences, Beijing 100190, China

Supporting Information

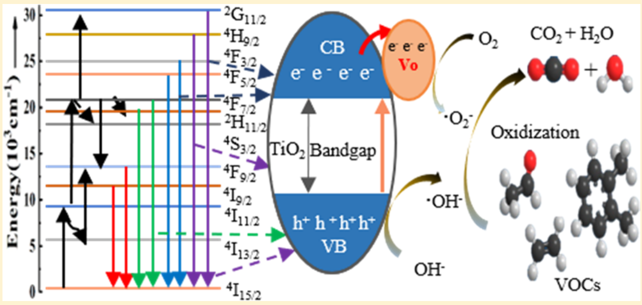

ABSTRACT: A series of Er-doped TiO_2 photocatalysts, using $Er(NO_3)_3{\cdot}6H_2O$ precursor ranging from 0.5 to 2 mol %, were synthesized via sol−gel method with titanium(IV) isopropoxide solution as reactant. The structure and properties of as-prepared samples were characterized by scanning electron microscopy, transmission electron microscopy, X-ray diffraction, UV−vis spectroscopy, X-ray photoelectron spectroscopy (XPS), Fourier transform infrared spectroscopy, thermogravimetric analysis, photoluminescence, electrochemical impedance spectroscopy, and photocurrent. The as-synthesized Er-doped TiO_2 nanoparticles demonstrated improved photocatalytic activities for the photodegradation of selected volatile organic compounds, including acetaldehyde, *o*-xylene, and ethylene. Additionally, high photodegradation of acetaldehyde was recorded in the visible region ($\lambda > 420$ nm). XPS analysis revealed that a handful of Er in anatase TiO_2 was presented in the form of Er_2O_3, which benefited by increasing the specific surface area ranging from 59.28 to 110.34 m^2/g and consequently enhanced the adsorption capacity for acetaldehyde, *o*-xylene, and ethylene 3.3, 3.7, and 3.8 times, respectively, in contrast to the undoped TiO_2. Electron spin resonance results showed that Er doping caused production of oxygen vacancies (V_O) and Ti^{3+}, which promoted the photocatalytic activity of the catalyst. The TiO_2 samples containing 0.5−1.5% Er content exhibited higher photoactivity in comparison with other samples. The highest removal efficiency of acetaldehyde and *o*-xylene within 100 min was 99.2 and 84.6%, respectively, and ethylene degradation efficiency reached 22.4% within 180 min. Furthermore, the visible light elimination efficiency of acetaldehyde was 25.5%. Finally, the results suggested that Er doping predominantly inhibited the catalyst poisoning in the degradation of *o*-xylene.

1. INTRODUCTION

A large number of volatile organic compounds (VOCs) cause urban smog and photochemical smog and pose serious health risks due to a carcinogenic−mutagenic nature; thus, the VOCs are strictly regulated by various industrial countries, for example, U.S., India, and China.[1−3] Therefore, the reduction of VOCs in the atmosphere is pivotal for environmental management and human health. At present, the treatment technologies for VOCs include thermal catalysis, ozone oxidation, adsorption, and photocatalysis.[4,5] Among them, photocatalytic technology provides opportunities for the treatment of VOCs due to its low energy consumption and high degradation efficiency.

Among many semiconductor photocatalytic materials, TiO_2 has been widely considered as a degrading pollutant (aqueous- and gas-phase photocatalytic degradation)[6−9] due to its nontoxicity, high oxidation potential, good photochemical stability, and good photocatalytic activity.[10,11] However, pure TiO_2 is rarely used in practical applications because of its low rate of light energy utilization and high recombination rate of photogenerated carriers. Therefore, rare earth elements are used to modify TiO_2 to expand the light harvesting region of TiO_2 and promote the charge separation efficiency thereby improving photocatalytic performance.[12,13] The rare earth element-doped metal oxides, for example, Er^{3+}-doped TiO_2, have been widely considered for optoelectrical applications;[14−20] however, most of the work is mainly focused on luminescent properties[14,15] or photocatalytic degradation of model dyes in solution.[17−20] Moreover, only a few reports exist on the photocatalytic degradation of gaseous pollutants for Er^{3+}-doped TiO_2, where the VOCs have been widely ignored. Similarly, liquid-phase bisphenol A was used to estimate the properties of a Fe/Er-TiO_2 photocatalyst prepared by Hou et al.,[21] which indicated an improved photocatalytic performance of Fe/Er-TiO_2 in comparison with pure TiO_2, Er-TiO_2, and Fe-TiO_2. Reszczynska et al.[22] synthesized Er^{3+}−TiO_2 samples

Received: March 5, 2019
Revised: April 20, 2019
Published: April 24, 2019

ACS Publications

DOI: 10.1021/acs.jpcc.9b02093
J. Phys. Chem. C 2019, 123, 12321−12334

by sol−gel method having good photoactivities for phenol in an aqueous solution. Both workers implied that the factors affecting the photocatalytic performance of the catalyst may be involved with defect states (Ti^{3+} and V_O). However, to the best of our knowledge, the effect of Er doping in TiO_2 and its crystal defect chemistry, such as the presence of oxygen vacancies (V_O) and reduced titanium ions ($Ti^{4+} \rightarrow Ti^{3+}$) on photocatalytic degradation of VOCs, has not been explored. Most importantly, in contrast to liquid-phase photocatalysis, the gas-phase photocatalysis involve the adsorption of gaseous pollutants on the catalyst surface, which further reacts with the active superoxide and hydroxyl radicals on the surface. These reactive radices further oxidized and decomposed the adsorbed gaseous VOC molecules into H_2O, CO_2, and other intermediates.[23−25] Various parameters, such as nature of the gas, flow rate, temperature, specific surface area, catalyst type, and light intensity, influence the photocatalytic activity. Therefore, it is important to prioritize the gaseous pollutant photodegradation to develop potential photocatalyst materials.

In this work, we have synthesized Er-doped TiO_2 to comprehend the photocatalytic activity for the photodegradation of VOCs. The effect of Er content on the crystal structure of TiO_2 and photocatalytic properties is discussed in depth. We utilized three model gaseous pollutants, including acetaldehyde, *o*-xylene, and ethylene, to evaluate the photocatalytic properties of Er-doped TiO_2. Among them, acetaldehyde and *o*-xylene are typical air pollutants that contain aldehyde a group and phenyl ring, respectively, whereas ethylene is released from fruits and one of the world's largest available chemical products that contains a carbon−carbon double bond. These VOCs can cause serious problems, for example, breathing problems, irritation, suffocation, narcotic effect, headache, cancer, and even death. Our study suggested that Er doping significantly improved the photocatalytic performance; the mechanism for the photodegradation of gaseous VOCs on the as-prepared photocatalyst was also proposed.

2. EXPERIMENTAL SECTION

2.1. Preparation of Er-TiO_2 Photocatalysts. The sol−gel method was used to synthesize pure and Er-doped TiO_2 nanoparticles. Initially, 9.8 mL of titanium(IV) isopropoxide (TIP) was dissolved in a mixture solution containing 42 mL of ethanol and 8 mL of acetic acid under vigorous stirring for 15 min. Next, 4 mL of distilled water was slowly dropped into the above solution under magnetic stirring. Furthermore, a predetermined amount of $Er(NO_3)_3 \cdot 6H_2O$ was added into the final mixture, which was further stirred for 80 min in a closed beaker to achieve a clear sol. The sol was aged for 1 h and dried in a vacuum oven at 80 °C for 15 h to obtain the dried gel. Finally, the gel was calcined in a muffle furnace at 500 °C for 2.5 h in air and subsequently grounded with an agate mortar to collect the final products. The products are designated as pure TiO_2 and with different mole ratio contents as 0.5%Er-TiO_2, 1%Er-TiO_2, 1.5%Er-TiO_2, and 2%Er-TiO_2, respectively.

All chemicals in our work, including acetic acid and ethanol (Zhenxing Co., Ltd., Shanghai), were used as received without further purification. Titanium(IV) isopropoxide (TIP), as the titanium source, was purchased from Sigma-Aldrich. $Er(NO_3)_3 \cdot 6H_2O$ (99.9%, Sigma-Aldrich) was used as the erbium-ion source. 5,5-Dimethyl-1-pyrroline *N*-oxide (DMPO) was obtained from Sigma Chemical Co. 2,2,6,6-Tetramethyl-1-piperidinyloxy (TEMPO) and *p*-benzoquinone (PBQ) were purchased from Aladdin Industrial Corporation.

2.2. Characterization. The morphology of as-prepared samples was characterized by using a field-emission scanning electron microscope (SEM) equipped with an energy-dispersive spectrometer (EDS) (Magellan 400). A high-resolution transmission electron microscope (HRTEM; JEOL/JEM-2100) with an acelerating voltage of 200 kV was used to analyze the microstructure. The X-ray diffraction (XRD) patterns were recorded on the Bruker D8 Advance diffractometer using Cu Ka irradiation (λ = 1.5406 Å) in the range of 2θ from 20 to 80° with steps of 0.02° and 30 s per step. The Brunauer−Emmett−Teller (BET) specific surface area (S_{BET}) of the samples was analyzed by nitrogen adsorption at 77 K on a Micromeritics ASAP 3000 apparatus. UV−vis spectra were collected on a PerkinElmer Lambda 950 spectrometer using $BaSO_4$ as a reference at wavelengths from 300 to 1200 nm. Raman spectra were recorded with a DXR spectrometer using an excitation laser wavelength of 532 nm at laser power of 0.1 mW. X-ray photoelectron spectroscopy (XPS) data was carried out on a PerkinElmer PHI-5000C ESCA system using monochromatic Mg Kα X-ray source, and the binding energies were calibrated with respect to the signal for adventitious carbon (binding energy = 284.6 eV).

The electron spin resonance (ESR) signals of oxygen vacancies (V_O) and Ti^{3+} were recorded on a JES-FA200 spectrometer at 103 K. Also ESR signals of radicals trapped by 5,5-dimethyl-1-pyrroline *N*-oxide (DMPO) were recorded on a JES-FA200 spectrometer. First, 5 mg of as-prepared powder was dissolved in a mixed dispersion liquid (containing 50 μL of DMPO and 5 mL of deionized water or ethanol, where deionized water dispersion for DMPO-•OH and ethanol dispersion for DMPO-•O_2^-, respectively) by ultrasonication for 10 min. Then, the mixture was irradiated by a 400 W xenon lamp for 4 min. Temperature-programmed desorption (TPD) analysis (ChemiSorb PCA-1200, Builder China) was used to evaluate the adsorption/desorption performance of the catalysts. Prior to the analysis, the sample (0.1 g) was placed in a U-shaped quartz tube and heated from room temperature up to 150 °C (a heating rate of 10 °C/min) for 30 min under a high-purity N_2 flow (30 mL/min) to purge the sample. After cooling to room temperature, the N_2 flow was switched to VOC (acetaldehyde, o-xylene, or ethylene, respectively) and maintained for 120 min and subsequently the sample was purged with N_2 for 20 min. Finally, the analysis was carried out from room temperature to 600 °C.

Fourier transform infrared (FTIR) spectra were obtained using a Thermo Fisher iN10 iZ10 infrared spectrophotometer with KBr as the reference in the range from 400 to 4000 cm^{-1}. Thermogravimetric analysis (TGA) was carried out by a STA-449C thermogravimetric analyzer. Photoluminescence (PL) spectra were taken using the PerkinElmer luminescence spectrometer 55 (LS55) equipped with a xenon lamp with an excition wavelength of 250 nm.

The transient photocurrent response curve and electrochemical impedance spectroscopy (EIS) of the as-prepared photocatalysts were measured by an electrochemical workstation (CHI660D) with an AM1.5G solar power system used as the light irradiation source at an ambient temperature and without any light irradiation source, respectively. First, a certain amount of the sample was dispersed in a certain amount of ethanol, and second, a certain amount of the dispersion liquid was taken out by a pipetting gun to be spin-

Scheme 1. Experimental Setup for Photocatalytic VOC Oxidation with Real-Time Monitoring and Testing

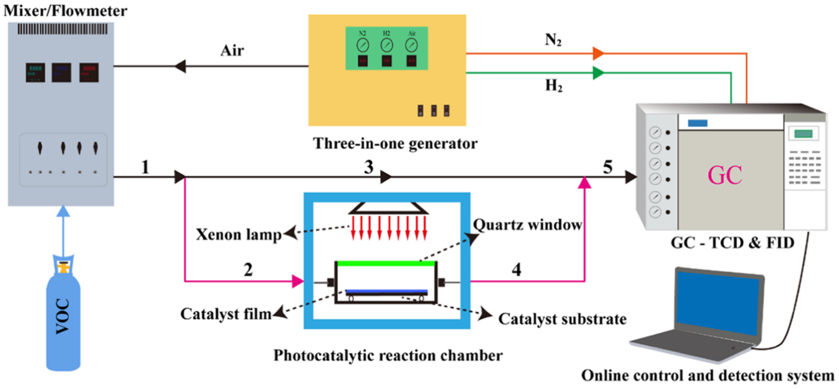

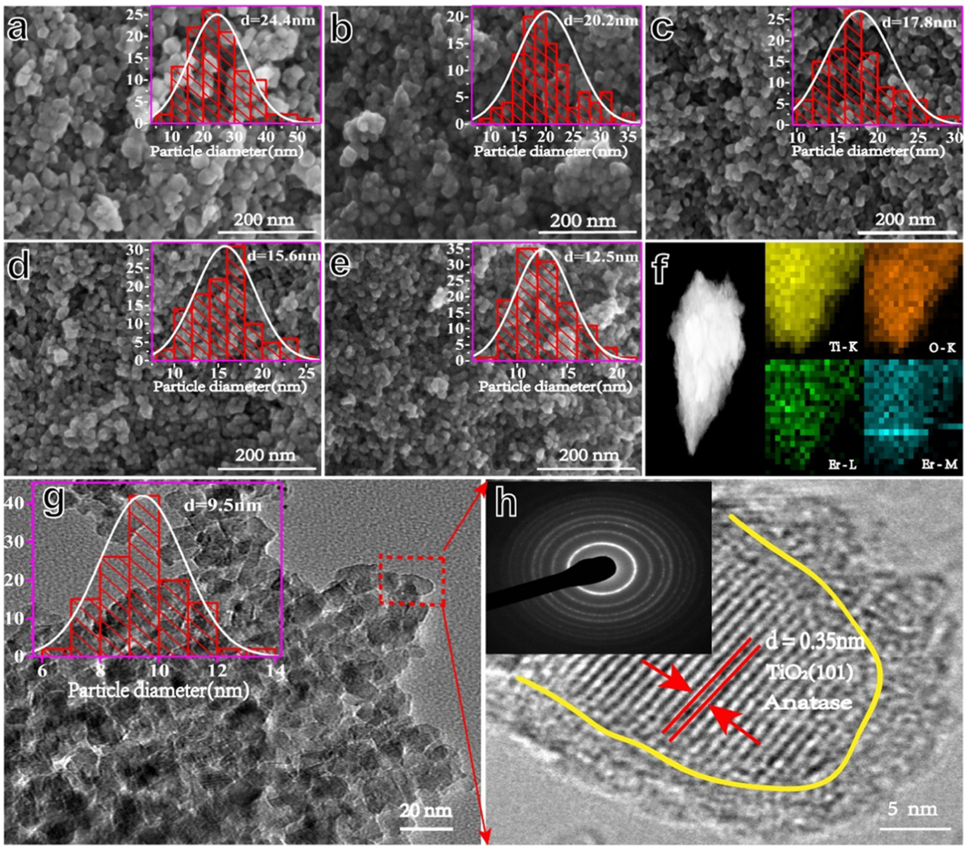

Figure 1. SEM images of (a) pure-TiO_2, (b) 0.5%Er-TiO_2, (c) 1%Er-TiO_2, (d) 1.5%Er-TiO_2, and (e) 2%Er-TiO_2 samples; the inset figures demonstrate particle size distribution of the corresponding samples; (f) shows selected area elemental mapping for the 2%Er-TiO_2 sample exhibiting spatially resolved elements of Ti, O, and Er, (g) TEM and (h) HRTEM images of 2%Er-TiO_2 sample; the inset in (g) is the histogram of catalyst nanoparticle size distribution.

coated on a fluorine-doped tin oxide (FTO) glass sheet of 1 cm × 2.5 cm and air-dried. Finally, the FTO glass, platinum electrode, and Ag/AgCl were used as the working electrode, counter electrode, and reference electrode, respectively. The photocurrent response curves and EIS were measured by putting them into a three-electrode quartz cell containing 1 M NaCl electrolyte and "0.1 M NaCl + 0.1 mM Fe^{2+} + 0.1 mM Fe^{3+}" electrolyte, respectively.

2.3. Adsorption Capacity and Photocatalytic Activity.

The adsorption and photodegradation of the target VOC gas were measured in a continuous automatic intake reactor under an ambient temperature (Scheme 1) for all samples. To analyze the adsorption behavior of pure and Er-doped TiO_2 photocatalysts, we conducted dynamic adsorption tests of gaseous acetaldehyde, *o*-xylene, and ethylene under a dark condition. The selected VOC mixed with dehydrated air in the mixer. Before starting the test, the mixed gas entered the gas chromatograghy (GC) through the black pipes 1, 3, and 5. The FID detector of GC could detect the concentration of the target VOC. During the adsorption and photodegradation tests, the mixed gas flowed into the reaction cell through the black pipe 1 and the red pipe 2 and was in contact with the photocatalyst in the rectangular chamber. Then, the residual gas in the chamber flowed into GC through the red pipe 4 and the black pipe 5 and the concentration of the contaminant was measured.

DOI: 10.1021/acs.jpcc.9b02093
J. Phys. Chem. C 2019, 123, 12321−12334

In a typical procedure, powders (100 mg) were dispersed in 1 mL of ethanol and sonicated for 1 h. Next, the mixed solution was uniformly applied on a glass substrate (16×13 cm^2) and air-dried. Finally, the samples were put into the photocatalytic reaction test system. The VOC gas (acetaldehyde or *o*-xylene, or ethylene, respectively) was introduced into the reaction chamber (flow rate: 20 sccm) for enough time to reach the adsorption−desorption equilibrium. In this experiment, the initial concentration of *o*-xylene and ethylene was 25 ppm and the initial concentration of acetaldehyde was 25 and 500 ppm, respectively. The adsorption capacity (Q) of the target VOC gas was calculated as follows

$$Q = C_0 \times \rho_1 \times \rho_2 \times [\int_0^t v \times (1 - C/C_0)\,dt]_{\text{catalyst}} - [\int_0^t v \times (1 - C/C_0)\,dt]_{\text{blank}}/(M \times m)$$

where C_0 and C are the concentration of VOC at the initial condition and different time intervals, ρ_1 is the air density, ρ_2 is the relative vapor density of gaseous VOC, v is the flow rate of target VOC gas, t is the time interval of reaction, M is the molar mass of VOC, and m is the mass of used catalyst, respectively.

The photocatalytic activity test can only be performed after the adsorption−desorption of target VOC on the material reaching equilibrium in the dark condition. A 400 W xenon lamp was used as a photodegradation radiation source. The visible light ($\lambda > 420$ nm) activity of the photocatalysts was evaluated by testing the efficiency of gaseous acetaldehyde. The conversion efficiency (φ) was calculated as $\varphi = (C_0 - C)/C_0 \times 100\%$. The kinetics of VOC photocatalytic reaction follows a pseudo-first-order kinetic model at 25 ppm as $-\ln(C_0/C) = kt$, where k is the reaction rate constant.

3. RESULTS AND DISCUSSION

3.1. Morphology and Structural Characteristics of Photocatalysts. The SEM analysis demonstrated well-connected grain growth exhibiting a somewhat spherical morphology for all samples. The mean particle size was observed to decrease from 20.2 to 12.5 nm with increasing Er content in comparison with undoped TiO_2 (24.4 nm) (Figure 1a−e), indicating that the introduction of erbium-ion doping significantly inhibited the grain growth. The agglomeration of TiO_2 particles was obvious, probably due to the interaction of small particles. Additionally, the linear distribution of various elements, including Ti, Er, and O elements, is shown in Figure 1f. The energy-dispersive X-ray mapping results suggest uniform distribution of Er content in TiO_2 nanoparticles. The TEM image shows that the particle size of 2%Er-TiO_2 sample was relatively uniform and the average size was 9.5 nm (Figure 1g). Finally, the calculated value (0.35 nm) for the lattice fringes spacing could be indexed to (101) crystal plane of anatase of the sample 2%Er-TiO_2 and the particle was surrounded by an amorphous layer (3−5 nm) (Figure 1h), illustrating that on the surface of as-prepared catalysts might exist defect states.[26]

XRD patterns show a well-crystallized single phase for all samples, which were indexed to the pure anatase phase (Figure 2a), whereas no secondary phases could be traced in the XRD profiles. Additionally, the Scherrer equation was used to calculate the average crystallite size listed in Table 1, which showed a significant decrease from 15.9 to 9.6 nm for increasing Er content. Since the ionic radii of Er^{3+} (0.89 Å) is larger than Ti^{4+} (0.605 Å), the doping Er on Ti site will expand the crystal lattice.[27] Moreover, due to this phenomenon, the XRD peaks would be shifted to low 2θ values, which could be clearly evidenced from the inset in Figure 2a. These results suggested that Er was successfully incorporated inside the TiO_2 crystal lattice under the given experimental conditions. Er_2O_3 (detected in XPS analysis) could not be identified in the XRD results, which might be due to small quantity well below the detection limit of XRD.[28] It has been previously reported that a small concentration of Er_2O_3 at the grain boundaries might inhibit the grain growth, which might be responsible for the successive decrease of the average particle size and hence the increasing values of the specific surface area from 59.28 to 110.34 m^2/g with increasing Er concentration (Table 1), further promoting the photocatalytic activity.[29]

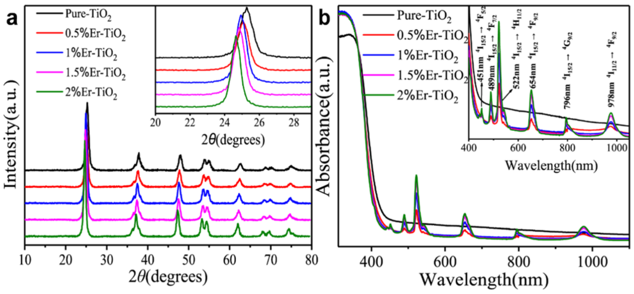

Figure 2. (a) XRD patterns and (b) UV−vis diffuse reflectance spectra of the as-prepared photocatalyst.

Table 1. Unit Cell Parameters and the Specific Surface Area for All Samples; the Value of *R* Profile in All Refinements Was below 12%

sample	a (Å)	c (Å)	V (Å^3)	crystallite size (nm)	S_{BET} (m^2/g)
pure-TiO_2	3.78905	9.51397	136.59	15.9	32.56
0.5%Er-TiO_2	3.79536	9.5125	137.03	13.4	59.28
1%Er-TiO_2	3.79531	9.51451	137.05	11.5	77.04
1.5%Er-TiO_2	3.79632	9.51125	137.08	10.4	97.89
2%Er-TiO_2	3.79699	9.54361	137.16	9.6	110.34

To further investigate the effect of Er on the crystal lattice of TiO_2, we calculated the lattice parameters utilizing the Rietveld refinement method, as given in Table 1. It can be observed that the expansion rate of the unit cell increases with Er amount. It was worth mentioning that there was no consensus in the literature on whether rare earth ions could replace the sites of titanium in the lattice or enter the lattice as interstitial defects. Some authors[30] suggested Eu and Sm ion incorporation in the anatase matrix. The Er ions have been reported to replace the Ti and stabilize the Ti−O bond in the TiO_2 crystal lattice.[31] Our results suggested that Er successfully occupied the Ti site in the crystal lattice; however, a small amount also resulted in the formation of the secondary phase, which was confirmed with the Raman and XPS analysis.

The optical properties of the pure and Er-doped samples were studied using UV−vis diffuse reflectance spectroscopy. As shown in Figure 2, the Er-doped TiO_2 exhibited absorption peaks ranging from 400 to 1100 nm in contrast to pure TiO_2. These adsorption peaks in the visible range were located at 451, 489, 522, 654, and 796 nm corresponding to transitions from the Er-ion ground state $^4I_{15/2}$ to the higher energy levels $^4F_{5/2}$, $^4F_{7/2}$, $^2H_{11/2}$, $^4F_{9/2}$, and $^4G_{9/2}$, respectively,[32] which might

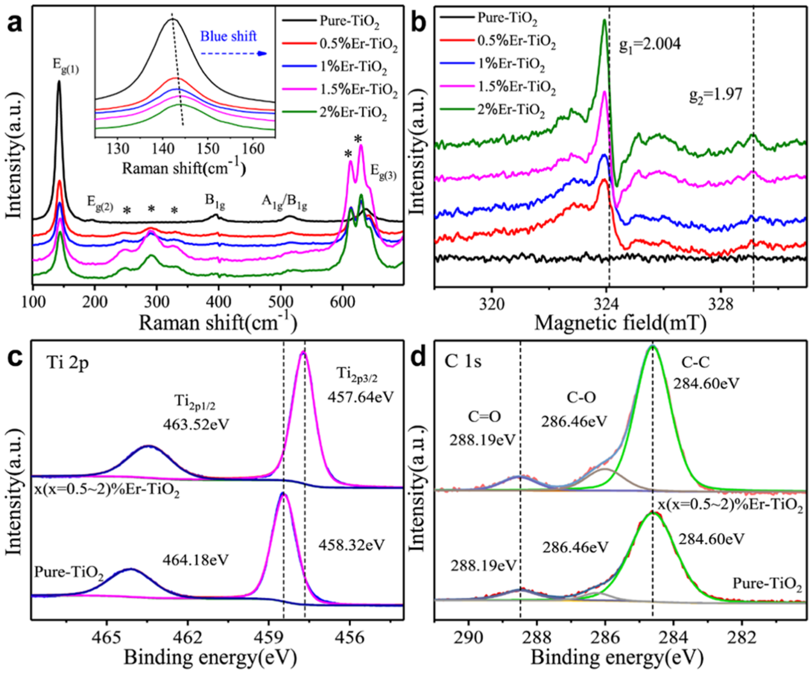

Figure 3. (a) Raman spectra of pure TiO_2 and Er-doped TiO_2 catalysts; the inset shows the enlarged spectrum at ~143 cm^{-1}; the XPS survey spectra of all samples in regions for (b) Ti 2p and (d) C 1s; (c) the ESR spectra of all photocatalysts at 103 K.

be associated with the upconversion. In addition, the absorption peak in the near-infrared (NIR) region (978 nm) could be related to the $^4I_{11/2}$ transition. In other words, Er-TiO_2 sample could significantly convert low-energy light into higher-energy light, such as red, green, and ultraviolet light. This was beneficial in increasing the light energy utilization of the catalyst while increasing the visible and near-infrared light response. Furthermore, all the Er-modified TiO_2 showed a blue shift compared with undoped TiO_2. This result contradicted the previous reports that have suggested red shift for similar systems.[20] However, the blue-shift phenomenon was more pronounced with the increase of Er content in our study, which might be due to decreasing grain size.[33] The relative intensity of the absorption peak increased with the increase of the amount of Er, which was beneficial to increasing the light utilization rate and improving the photocatalytic performance.

Raman spectroscopy was used to investigate the structural characteristics of pure and Er-doped TiO_2 (Figure 3a). All samples exhibited Raman bands at ~143, 195, 395, 515, and 637 cm^{-1} corresponding to $E_{g(1)}$, $E_{g(2)}$, B_{1g}, A_{1g}/B_{1g}, and $E_{g(3)}$ vibrational modes of TiO_2, respectively, in which E_g, B_{1g}, and A_{1g} bands were respectively associated to symmetric stretching, asymmetric and symmetric bending vibrations of O−Ti−O.[33,34] It could be noted that there existed new Raman bands located at 248, 290, 331, 617, and 628 cm^{-1} appearing in Er-doped TiO_2 in the range of 100−700 cm^{-1} compared with pure TiO_2 sample. To the best of our knowledge, there was no relevant literature to report on this case. The reason for this was that the incorporation of Er caused the evolution of TiO_2 structure and the production of defects. Furthermore, the relative intensity of the Raman peak ($E_{g(1)}$) decreased on increasing the amount of Er, indicating that the Ti center in the anatase crystal lattice was distorted, which consequently produced defects (V_O or Ti^{3+}). The evolution of E_g mode could be used as a direct evidence for the existence of defects (V_O or Ti^{3+}) in a tetragonal system,[35] where the E_g mode was more sensitive to oxygen deficiencies than the Ti−O stretching mode. The existence of a blue shift of the Raman peak ($E_{g(1)}$ ~ 143 cm^{-1}) was shown in the inset Figure 3a, which confirmed the presence of defects (V_O or Ti^{3+}).[26]

Electron spin resonance (ESR) has been widely used as a direct characterization technique to confirm the existence of V_O and Ti^{3+} in TiO_2. Figure 3b showed the ESR signals for all samples at 103 K. However, no clear ESR signals could be traced in pure TiO_2. The signal at g_1 = 2.004 appeared in Er-doped TiO_2, which could be assigned to the production of V_O or O^- anion radicals.[36] Furthermore, a weaker ESR signal at g_2 = 1.9712 for the Er-doped TiO_2 samples was observed, which could be associated with the presence of Ti^{3+}.[3737] Therefore, it could be concluded that the introduction of Er in TiO_2 lead to generating V_O and Ti^{3+}. Finally, the intensity of these signals was observed to increase with increasing Er content, demonstrating that the number of defects (V_O) increased, which played an important role in the photocatalytic properties.

X-ray photoelectron spectroscopy (XPS) was carried out to further examine the surface features of TiO_2-based samples. As given in Figure 3c, the peaks around 458.32 and 464.18 eV correspond to Ti $2p_{3/2}$ and Ti $2p_{1/2}$ of typical Ti^{4+}−O bonds in TiO_2, respectively.[38] It was observed that the Ti 2p peaks for all Er-doped TiO_2 moved toward low binding energy in contrast to TiO_2 wherein two peaks located at 457.64 and 463.52 eV, corresponding to Ti $2p_{3/2}$ and Ti $2p_{1/2}$ of Ti^{3+}, respectively, confirmed the formation of relatively stable Ti^{3+} in TiO_2,[39] which was in agreement with the Raman and ESR data.

Additionally, three peaks of C 1s XPS spectra were observed at 284.60, 286.46, and 288.19 eV, which could be associated with C−C, C−OH, and C═O, respectively (Figure 3d).[40] The presence of carbonaceous species in XPS spectra might be due to the atmospheric gas adsorption and organic residues during calcination process.[41] The concentration of carbonaceous

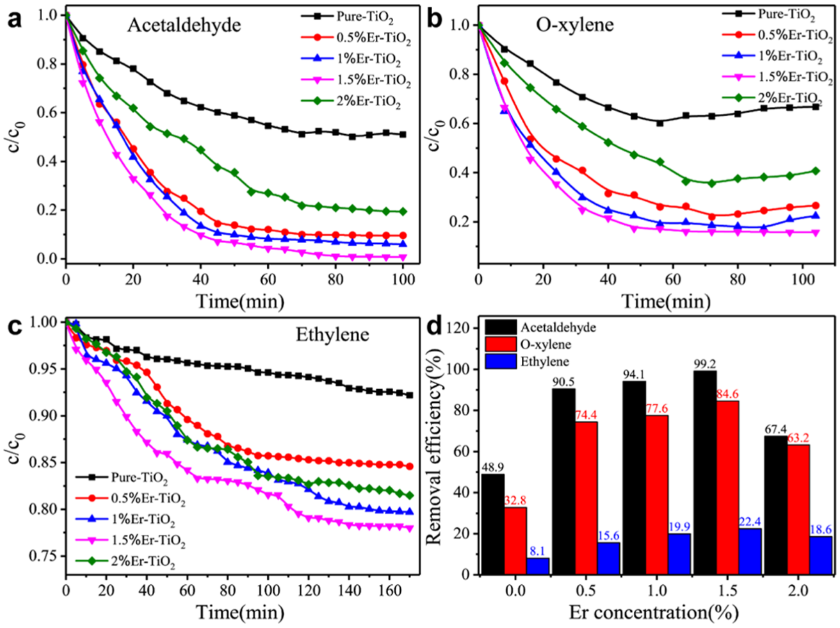

Figure 4. Degradation curves of (a) acetaldehyde, (b) *o*-xylene, and (c) ethylene under the radiation of a 400 W xenon lamp of 0.1 g photocatalysts, and (d) comparative histogram of degradation efficiency of different VOCs.

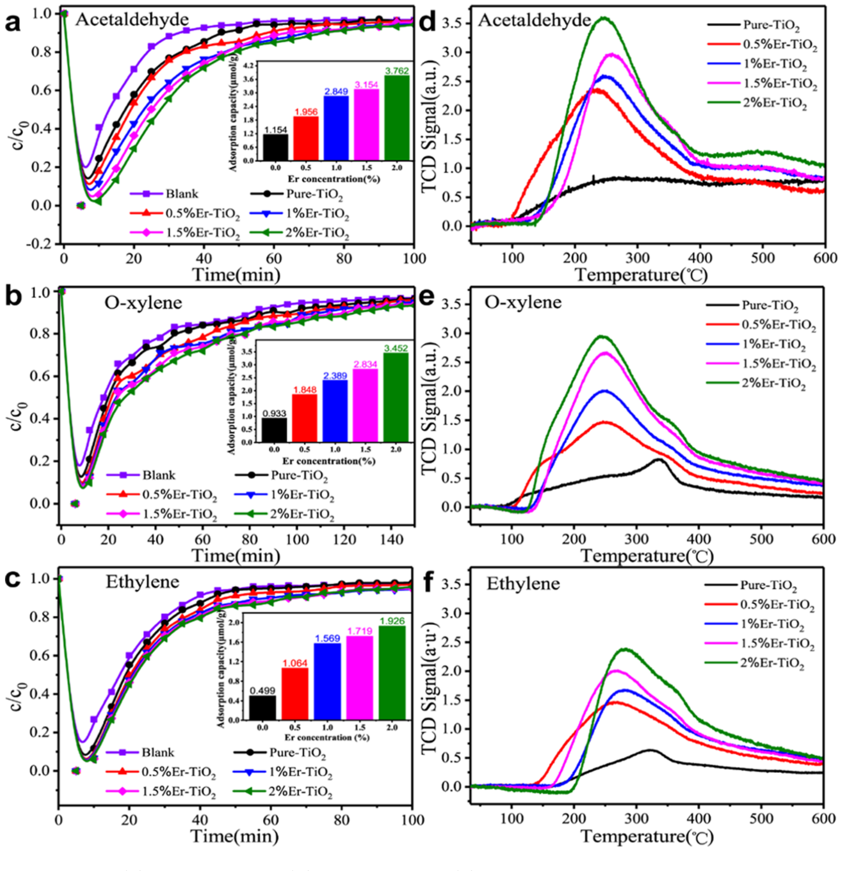

Figure 5. Adsorption dynamic curve of (a) acetaldehyde, (b) *o*-xylene, and (c) ethylene, 0.1 g, as-synthesized catalysts in the dark condition (the inset is the saturated adsorption capacity of the corresponding gaseous VOC) and (d) acetaldehyde-TPD, (e) *o*-xylene-TPD, and (f) ethylene-TPD, 0.1 g, as-synthesized catalysts and the concentration of all VOCs is 25 ppm.

species increases with the increase of erbium content (Table S1), which might have an effect on the photocatalytic performance of the catalyst. The TGA analysis and FTIR study further confirmed these results. A broad peak with an additional shoulder of O 1s XPS spectra could be resolved into two peaks, at ~529.03 and ~531.38 eV, assigned to surface lattice oxygen (O_L) and surface Ti−OH groups (O_{OH}), respectively (Figure S1a).[42] The ratio of $O_{OH}/(O_{OH} + O_L)$ increased from 0.08 to 0.28 on increasing the content of Er (Table S1), demonstrating that the surface hydrophilicity of

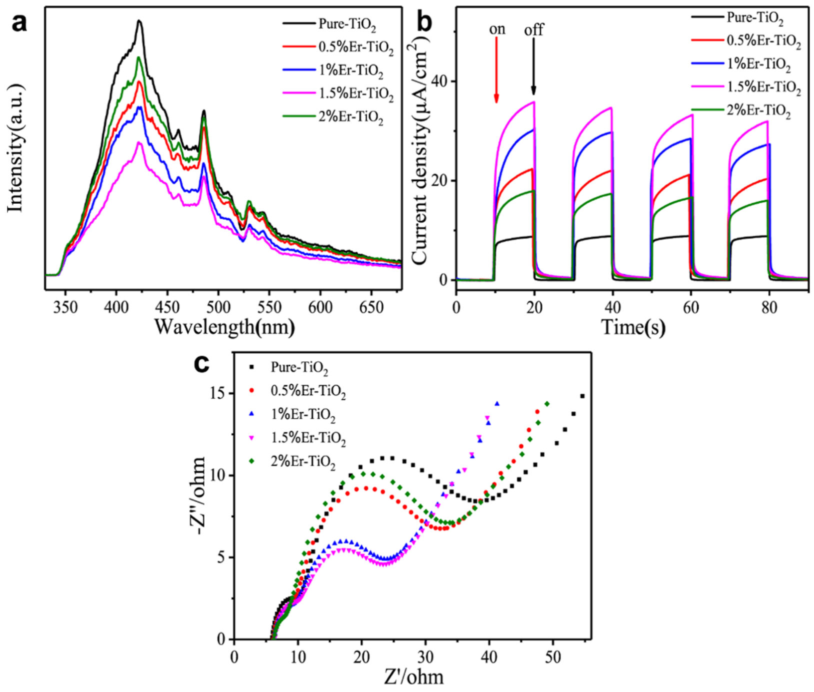

Figure 6. (a) Photoluminescence spectra excited at 250 nm, (b) transient photocurrent response curves, and (b) electrochemical impedance curves of TiO_2 doping with Er samples and bare TiO_2 sample.

the catalyst was enhanced, thereby further influencing the photocatalytic activity.[43] Moreover, the concentration of O_{OH} not only could be indirectly related to the formation of V_O but also might stabilize the lattice disorder by passivating the dangling bonds,[44] resulting in improving the photocatalytic performance. Figure S1b presented Er 4d XPS peak located at ~168.79 eV, which could be attributed to Er−O of Er_2O_3,[4545] which evidenced the presence of Er_2O_3 on the surface of Er-doped TiO_2 samples.

3.2. Photocatalytic Performances and Their Influencing Factors. Considering above results, three kinds of typical gaseous VOCs experiment to evaluate the photocatalytic activity of pure and Er-doped TiO_2. Photodegradation curves for the flowing gas-phase acetaldehyde (25 ppm, 20 sccm) are shown in Figure 4a. It can be seen that all the Er^{3+}-doped TiO_2 samples exhibited superior photocatalytic performance in contrast to undoped TiO_2, which suggests that Er doping was an efficient way to enhance the photocatalytic properties of TiO_2. Meanwhile, the order of removal efficiency of acetaldehyde for different samples could be as follows (Figure 4d): 1.5%Er-TiO_2 (99.2%) > 1%Er-TiO_2 (94.1%) > 0.5%Er-TiO_2 (90.5%) > 2%Er-TiO_2 (67.4%) > pure-TiO_2 (48.9%). Photodegradation curves of *o*-xylene are presented in Figure 4b (25 ppm, 20 sccm); the photocatalytic properties of Er^{3+}-modified TiO_2 catalysts improved significantly. The photocatalytic efficiency of pure-TiO_2, 0.5%Er-TiO_2, 1%Er-TiO_2, 1.5%Er-TiO_2, and 2%Er-TiO_2 for *o*-xylene was recorded as 32.8, 74.4, 77.6, 84.6, and 63.2% (Figure 4d), respectively. Similar trends could be observed from the degradation curves of *o*-xylene, as shown in Figure 4b,d (25 ppm, 20 sccm). However, there were still significant differences in terms of degradation efficiency and rate (Figure S2). Additionally, the samples demonstrated a poor photocatalytic activity for ethylene. As can be seen from Figure 4c (25 ppm, 20 sccm), it was obvious that the order of photocatalytic efficiency for ethylene was as follows (Figure 4d): 1.5%Er-TiO_2 (22.4%) > 1%Er-TiO_2 (19.9%) > 2%Er-TiO_2 (18.6%) > 0.5%Er-TiO_2 (15.6%) > pure-TiO_2 (8.1%). Notably, it was found that the degradation principles of ethylene were slightly different from those of acetaldehyde and *o*-xylene. which could be attributed to the poor adsorption of ethylene molecules on the catalyst surface compared with acetaldehyde and *o*-xylene. A detailed discussion has been presented below. The optimum concentration of erbium ion exhibiting the best photocatalytic activity among the samples studied in this work was 1.5%, wherein the photodegradation efficiency and rate constant of acetaldehyde were higher than those of *o*-xylene whereas minimum for ethylene (Figures 4d and S2). The difference in molecular weight and structure of the three VOCs lead to the above degradation conditions. It was well known that the energy required to break the C═C (607 kJ/mol) bond of ethylene and *o*-xylene is higher than that of the C−C (345.6 kJ/mol) and C−H (414 kJ/mol) bond of acetaldehyde.

It has been well established that the adsorption of the gas molecules to the surface is a crucial step for the surface-catalyzed photocatalytic reactions. On one hand, the difference of degradation results was related to the molecular structure of VOC, and on the other hand, it was also related to the adsorption state of VOCs on the catalyst surface. Therefore, we further investigated the adsorption capacity of the as-prepared photocatalysts for three different structures of VOCs through dynamic adsorption and TPD curves. The dynamic adsorption curves of acetaldehyde, *o*-xylene, and ethylene are presented in Figure 5a−c (25 ppm, 20 sccm), where the inset was the corresponding calculated adsorption capacity. It was clear from the results that the adsorption capacity of the catalyst increases with increasing Er content for the same VOC, which might be associated with the increasing specific surface area. All of the three model VOCs showed the highest adsorption amount on sample 2%Er-TiO_2, which was 2.3, 2.7, and 2.8 times increased for acetaldehyde, *o*-xylene, and ethylene, respectively. Among them, the highest adsorption

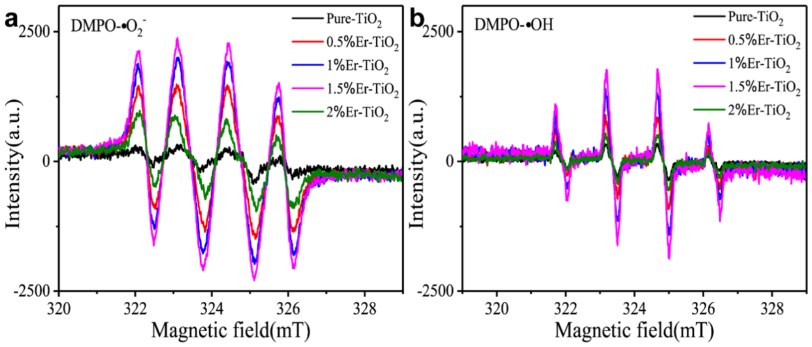

Figure 7. ESR signals of DMPO-●O_2^- in ethanol dispersion (a) and DMPO-●OH in aqueous dispersion (b) of as-prepared photocatalysts under 400 W xenon lamp irradiation for 4 min.

capacity is of acetaldehyde whereas the lowest adsorption capacity is of ethylene, illustrating that acetaldehyde is more easily adsorbed on the catalyst surface in comparison with *o*-xylene and ethylene. One reason was that small molecule acetaldehyde was more easily adsorbed on the surface of TiO_2 compared with the larger one that was more easily adsorbed on the surface of TiO_2 compared with larger molecule *o*-xylene. Another reason was the polarity of both the gaseous pollutants and the photocatalysts. Er-doped TiO_2 has more polar surface (as shown in Table S1, which has a higher ratio of O_{OH}), which adsorbed polar pollutants more easily than nonpolar molecular pollutants.[46] It was quite easy to understand that the sample has a much higher adsorption capacity for acetaldehyde and *o*-xylene than ethylene. Further evidence from the TPD data is shown in Figure 5d−f. A similar desorption peak, located at 110−420 °C, was observed in acetaldehyde, *o*-xylene, and ethylene TPD curves. A weak desorption peak appeared for acetaldehyde in pure TiO_2, whereas strong desorption peaks appeared for all Er-doped TiO_2 catalysts. The adsorption capacity of acetaldehyde and *o*-xylene was far greater than that of ethylene. This result was highly consistent with the dynamic adsorption curve. Meanwhile, it could be observed that the desorption peaks of pure TiO_2 for *o*-xylene (Figure 5e) and ethylene (Figure 5f) were, respectively, at 337 and 323 °C, which were higher than those of Er-TiO_2 samples (respectively, located at ∼246 and ∼277 °C), indicating that pure TiO_2 had strong chemisorption. The chemical adsorption of ethylene (∼277 °C) for the sample was stronger than that of *o*-xylene (∼246 °C) and acetaldehyde (∼235 °C). Therefore, it was speculated that the incorporation of Er contributed to the adsorption of VOCs and changed the adsorption state of VOCs, further affecting the photocatalytic performance.

The photocatalytic performance of the catalyst was not only related to adsorption properties but also to the separation efficiency of the electron−hole pairs. To further understand the role of defects in TiO_2-based samples for trapping, mobility, and recombination of photogenerated charge carriers of photoinduced electron−hole pairs under the existence of defects in TiO_2, we performed photoluminescence (PL) and photoelectrochemical tests. PL emission spectra revealed that the intensity of the Er-doped TiO_2 samples was lower than that of undoped TiO_2, demonstrating that the separation of photogenerated carriers of catalyst was promoted (Figure 6a). This was attributed to the introduction of Er in TiO_2 to generate defects (V_O, Ti^{3+}) capturing photoinduced electrons[47] and intra-4f electrons of Er ion, accelerating photogenerated charge-transfer transition between TiO_2 and Er ion,[48] which could effectively increase the generation of degradation actives, thus enhancing the photocatalytic activity of the photocatalysts. The intensity of PL signals for as-synthesized samples decreased with increasing Er content in the range of 0.5−1.5% in our study. However, it was noticed that the intensity of 2%Er-TiO_2 sample was higher than that of 0.5%Er-TiO_2, illustrating that the separation process of photogenerated carriers was suppressed, which could be attributed to the existence of V_O. Combined with ESR analysis, it could be inferred that the excess V_O in the 2%Er-TiO_2 sample acted as the recombination center for photo-induced carriers,[49] which was in good agreement with photocatalytic degradation test curves.

The photocurrent density curve and electrochemical impedance spectroscopy (EIS) can also be used to understand the separation efficiency of photogenerated electron−hole pairs on the catalyst surface. Photocurrent response curves for TiO_2-based samples were presented in Figure 6b. The experiments were performed under chopped conditions both in the dark and light. The photocurrent density of as-prepared photocatalysts increased with an increasing amount of Er, demonstrating that the charge separation efficiency significantly improved. Furthermore, the excess V_O acted as a recombination center, promoting the recombination of electron−hole pairs. The photocurrent decay of 2%Er-TiO_2 sample provided a direct evidence for this behavior, which was consistent with the PL results.

The EIS analysis further confirmed these results. As shown in Figure 6c, the Nyquist plots of catalysts consist of two separated semicircles and a sloping line in the frequency range of 1 Hz to 100 kHz.[39] The larger the radius of the EIS Nyquist plots, the weaker is the separation efficiency of electron−hole pairs. It was observed that the radius of the Nyquist plots for pure TiO_2 sample was the largest among all catalysts whereas that of the 1.5%Er-TiO_2 catalyst was the smallest, demonstrating that the separation efficiency of photogenerated carriers of Er-incorporated samples improved and doping with 1.5% Er gave the most excellent result. Therefore, the above results suggest that all doped samples had a faster charge-transfer and separation rate in comparison with undoped TiO_2. Remarkably, in the photodegradation process of ethylene, although the photogenerated charge separation of 0.5%Er-TiO_2 sample was higher than that of the 2%Er-TiO_2 sample, the photocatalytic activity of 0.5%Er-TiO_2 sample was poorer than that of 2%Er-TiO_2 sample, which could be ascribed to the adsorption capacity of 2%Er-TiO_2 sample being significantly higher than that of 0.5%Er-TiO_2 sample, Thus, combined with photocatalytic performance, adsorption capacity, and photogenerated charge separation efficiency, it could be concluded that

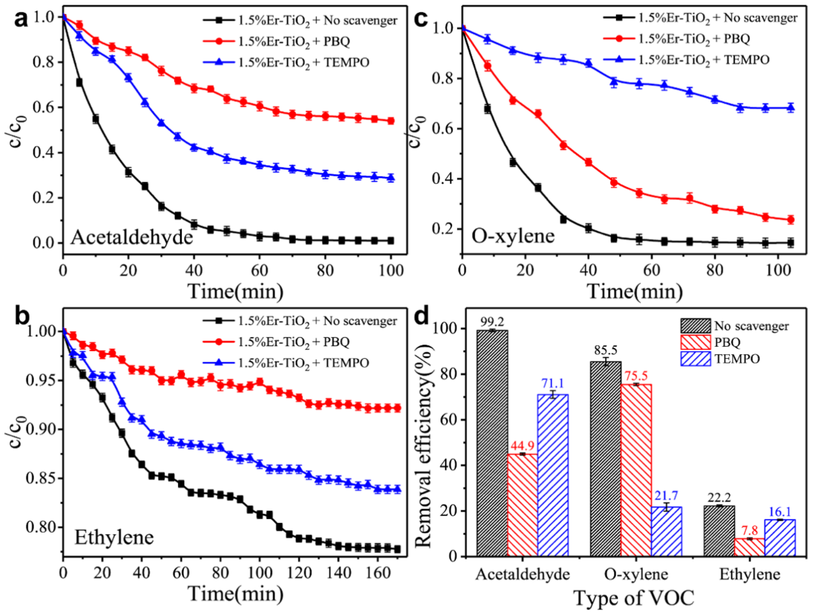

Figure 8. Plots of active species trapping on photocatalytic degradation of (a) acetaldehyde, (b) ethylene, and (c) *o*-xylene of 1.5%Er-TiO$_2$ sample; (d) comparative histogram of the degradation efficiency of different VOCs under different active species in which TEMPO acts as an •OH trapping agent and PBQ acting as an •O_2^- trapping agent.

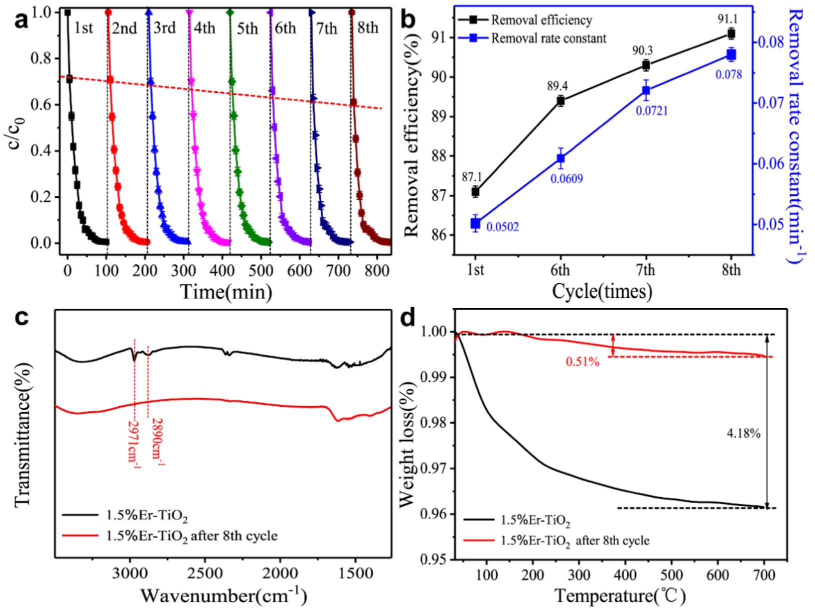

Figure 9. (a) Eight-cycle degradation curve; (b) degradation efficiency, and photodegradation rate constant of the first, sixth, seventh, and eighth cycle of the 25 ppm acetaldehyde eight-cycle degradation curve within 40 min of 1.5% Er-TiO$_2$ sample; (c) FTIR spectra and (d) TG curves before and after degradation of acetaldehyde of 1.5%Er-TiO$_2$ sample.

photocatalytic performance was relevant to the adsorption capacity. That is to say, the adsorption capacity of 2%Er-TiO$_2$ catalyst was the dominant factor affecting the photocatalytic activity when the photocatalytic efficiency was low in our case. This was why the photocatalytic efficiency of 2%Er-TiO$_2$ sample was higher than that of 0.5%Er-TiO$_2$ sample. On the basis of the above results, it could be concluded that the main factor affecting photocatalytic performance in photocatalysts was the generation and separation efficiency of photogenerated carriers.

We further detected the generation of active species (hydroxyl radicals (•OH), superoxide radicals (•O_2^-)) to disclose their functions on photocatalytic properties and photocatalytic processes. The 5,5-dimethyl-1-pyrroline *N*-oxide (DMPO) spin-trapping ESR technique was used to investigate the free radical active species formed during the removal of typical VOCs of as-prepared catalysts, as presented in Figure 7. The four-line ESR signals with characteristic intensity ratios of 1:2:2:1 for DMPO-•OH adducts and 1:1:1:1 for DMPO-•O_2^- adducts were, respectively, observed,[50] indicating that there exist hydroxyl radicals and superoxide radical active species involved in the removal of VOCs. In addition, it was observed that both free radical intensities increased with increasing Er concentration compared with pure

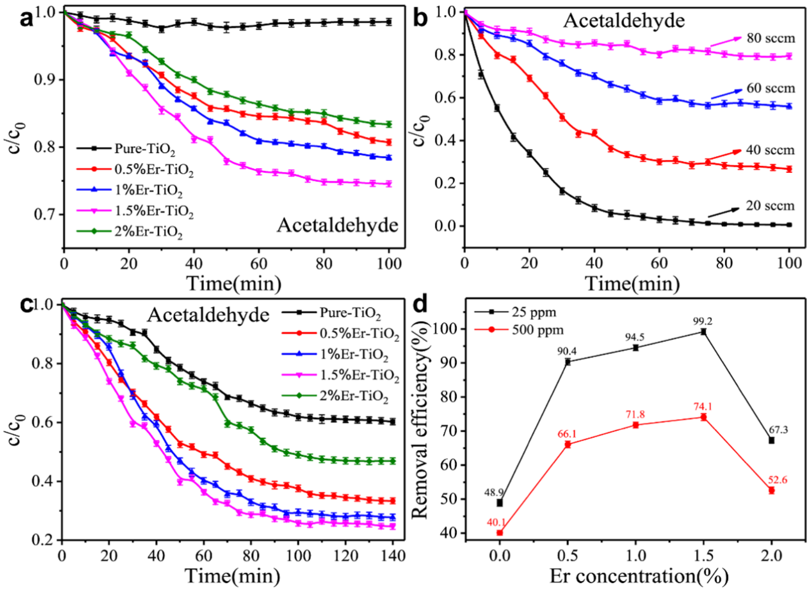

Figure 10. Degradation curves of 25 ppm acetaldehyde of 1.5% Er-TiO$_2$ sample under (a) visible light and (b) different flow rates; (c) the plots of photocatalytic degradation and (d) degradation efficiency and photodegradation rate constant of 500 ppm acetaldehyde of all catalysts.

TiO$_2$, benefiting from defects (V_O and Ti^{3+}) and the special intra-4f electronic structure of Er to promote the separation of electron−hole pairs, as well as the increase of OH groups (Table S1) on the TiO$_2$ surface after Er doping leading to the formation of •OH radicals. Moreover, among all doped samples, 1.5% Er-TiO$_2$ sample had the most •OH radicals and •O_2^- radicals whereas the 2% Er-TiO$_2$ sample had the least, which was consistent with PL spectra, photoelectrochemical curves, and photocatalytic activity test results. In addition, it was worth noting that the intensity of DMPO-•O_2^- yields (Figure 7a) was much stronger than that of DMPO-•OH (Figure 7b), attributed to the produced defects (V_O) favoring O_2 adsorption, further generating •O_2^- radicals.[51] To further investigate that which free radicals played a leading role, we performed a sacrificial capture experiment of 1.5%Er-TiO$_2$, of which *p*-benzoquinone (PBQ) and 2,2,6,6-tetramethyl-1-piperidinyloxy (TEMPO) were, respectively, applied to quench •O_2^- and •OH.[52,53] As shown in Figure 8a, it could be observed that the removal efficiency of acetaldehyde decreased from 99.2 to 44.9 and 71.1% (Figure 8d) after •O_2^- and •OH were scavenged by PBQ and TEMPO, respectively, suggesting that •O_2^- acted as the predominant active species throughout the process of photodegradation of gaseous acetaldehyde compared with •OH. A similar rule could be observed from the scavenger experiments of ethylene, as revealed in Figure 8b. When PBQ and TEMPO were applied, the photocatalytic efficiency decreased from 22.2 to 7.8 and 16.1% in the process of photocatalytic removal of ethylene (Figure 8d), respectively. Notably, the photodecomposition efficiency of gas-phase *o*-xylene decreased from 85.5 to 75.5 and 21.7% when PBQ and TEMPO were used (Figure 8c,d), demonstrating that •OH were the dominant active free radical. Hence, it could be concluded that •O_2^- and •OH play different roles in the photocatalytic degradation of these three kinds of VOC. Therefore, we could control the proportion of photoactive species in the catalyst for different VOCs. Also, we could selectively photodegrade the VOC system according to the content of reactive free radicals in the catalyst. For example, the catalyst has more •OH and such catalysts could be used to decompose benzene gas-phase pollutants whereas the catalyst with more •O_2^- could be used to remove aldehydes, olefins, and other gaseous pollutants, which provides ideas for a further in-depth research by follow-up work.

Considering the practical application of photocatalysts, we had investigated the stability, the visible light response of the catalyst, as well as the photodegradation characteristics of gas pollutants at different flow rates and concentrations. Stability and repeatable utilization are important for a photocatalyst in practical applications. 1.5% Er-TiO$_2$ was selected for the cyclic photodegradation experiment of acetaldehyde. Figure 9a showed that the photocatalyst still maintains excellent photocatalytic activity after eight cycles of degradation of acetaldehyde. It was noticeable that the photocatalytic performance (removal efficiency and rate) of the catalyst became better and better after the sixth cycle (Figure 9b). The reason for this result was probably that 1.5%Er-TiO$_2$ catalyst contained a small amount of carbonaceous species (2890 and 2971 cm^{-1}) occupying a part of the active site of the catalyst surface (Figure 9c) before the photocatalytic degradation of acetaldehyde[54] and the carbonaceous species disappeared in the catalyst after eight cycles of photocatalytic degradation of acetaldehyde. TGA curves further confirmed this suggestion (Figure 9d). The mass loss of the as-prepared catalyst (1.5% Er-TiO$_2$) was 4.18% after being calcinated at 500 °C, indicating the presence of carbonaceous species in the catalyst. After eight cycles of acetaldehyde photodegradation, the mass loss of the catalyst was 0.51%, showing that 3.67% of organic matter in the catalyst was removed. Therefore, the catalytic activity was getting better and better due to the prepared catalyst containing a small amount of carbonaceous species, which was decomposed, and more active sites being available after cyclic photolysis.

It was known from the UV−vis diffuse reflectance spectroscopy that the Er-doped TiO$_2$ catalysts exhibited significant absorption bands in the visible and near-infrared regions, which might favor a visible light response of the photocatalyst. Among the three kinds of VOCs, acetaldehyde was most susceptible to degradation, thereby acetaldehyde was

Scheme 2. Schematic Diagram of the Mechanism of Intra-4f Electron Structure of Er^{3+} and V_O Promoting Electron-to-Electron Transfer Enhancement and Upconversion Enhanced Light Energy Utilization

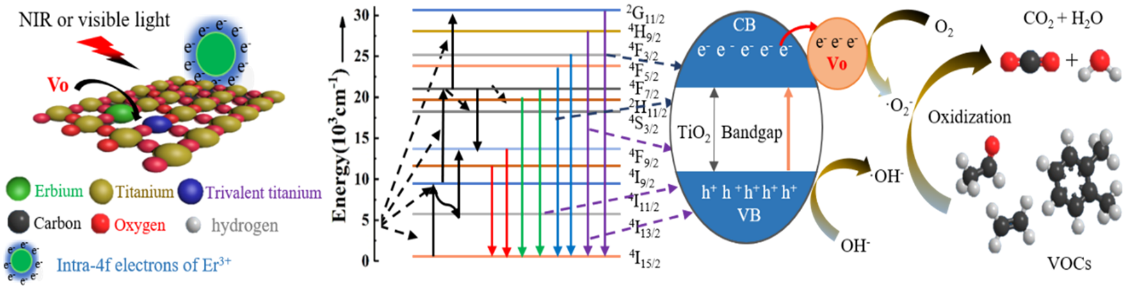

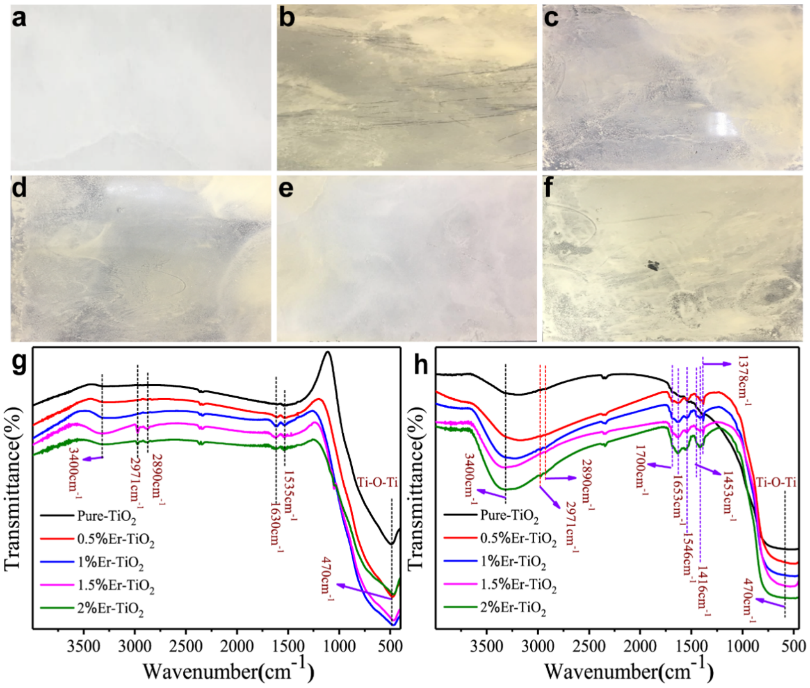

Figure 11. (a) Surface color of the as-prepared catalyst coating and surface color change of a series of TiO_2 samples after photocatalytic degradation of *o*-xylene: (b) pure-TiO_2, (c) 0.5%Er-TiO_2, (d) 1%Er-TiO_2, (e) 1.5%Er-TiO_2, and (f) 2%Er-TiO_2; the FTIR spectra of all samples (g) before and (h) after photocatalytic degradation of *o*-xylene.

selected for visible light ($\lambda > 420$ nm) activity testing (Figures 10a and S3a). Compared with pure TiO_2 (0%), Er-modified TiO_2 samples displayed visible light response, and when the amount of Er was 1.5%, the highest visible light degradation efficiency reached 25.5%. This was ascribed to upconversion characteristics of Er ion, which could adsorb visible and NIR light to convert high-energy light (UV) supporting TiO_2 utilization.[55] Nevertheless, the catalytic activity of 2%Er-TiO_2 sample with the largest defects (V_O) was lower than that of 0.5%Er-TiO_2 sample with the least defects (V_O), which was attributed to the large number of defect states serving as recombination centers, promoting the recombination of electron−hole pairs.

Furthermore, gaseous acetaldehyde was used as a target pollutant to explore the photocatalytic degradation characteristics at different flow rates. As the flow rate of gaseous contaminants increased from 20 to 80 sccm (Figure 10b), the photodegradation efficiency and rate of the catalyst gradually decreased from 99.2 to 20.6% (Figure S3b) and 0.065 to 0.050 min^{-1} (Figure S3c), respectively. This was attributed to the fact that the faster the flow rate of gaseous pollutants, the shorter is the contact time with catalysts and light, thus affecting the dynamic adsorption and photodegradation reactions in the photocatalytic process, resulting in a decrease in photocatalytic activity. Moreover, in the degradation curve of 500 ppm acetaldehyde (Figures 10c,d and S3d), it could be observed that the removal efficiency and degradation rate of acetaldehyde at a concentration of 25 ppm were higher than those of acetaldehyde at a concentration of 500 ppm. This was because a high concentration of acetaldehyde (500 ppm) adsorbed on the surface of the catalyst and covered some active sites of catalysts compared with a low concentration of acetaldehyde (25 ppm). On the basis of the above discussion and analysis, in practical applications, we should select the proper light source and set up a suitable concentration and flow rate of VOCs for degradation.

3.3. Proposed Mechanism. Considering the above experimental results and discussion, including microstructure, defect chemistry, hole−electron recombination process, production of photoactive species, and photocatalytic efficiency, a mechanism has been proposed in the following passage for the TiO_2-based samples. As presented in Scheme 2, light irradiation caused electronic transition of the photogenerated electrons from the valence band (VB) to the

DOI: 10.1021/acs.jpcc.9b02093
J. Phys. Chem. C 2019, 123, 12321−12334

conduction band (CB) in semiconductor photocatalysts (TiO_2), which reacted with the surface O_2 to form $\bullet O_2^-$. Similarly, the holes were created in the VB, which reacted with OH adsorbed on the surface to form •OH. These reactive radicals further oxidized and decomposed the adsorbed gas-phase VOC molecules into H_2O, CO_2, and other intermediates.[23−25] Remarkably, in the process of photodegradation of *o*-xylene, the catalyst was gradually deactivated with time (Figure 4b) and pure TiO_2 was first inactivated, indicating that the incorporation of Er could improve the photocatalyst durability. Moreover, the amount of yellow substance (intermediates) formed on the surface of the catalyst corresponded to the catalytic deactivation conditions (Figure 11a−f), wherein pure TiO_2 produced the most yellow matter. Therefore, the yellow matter was the chief culprit in catalyst poisoning, which was consistent with previous reports.[56] It was known from the FTIR spectrum analysis that some new bands appeared after photodegradation of *o*-xylene (Figure 11g,h), including 1378, 1416, 1453, 1546, 1653, and 1700 cm^{-1}. A small peak at 1378 cm^{-1} (ring stretchings, CH deformations) was attributed to adsorbed toluene on the catalyst surface;[57] the 1416 and 1453 cm^{-1} bands were assigned to the asymmetric and symmetric methyl bending vibrations.[58] The bands at 1546 and 1653 cm^{-1} (C═O) were associated with *o*-toluic acid and *o*-benzoate ion,[56] and a peak at 1700 cm^{-1} (C═O) could be assigned to adsorbed *o*-benzaldehyde.[56,58] Besides, the yellow intermediate products, including *o*-benzaldehyde, *o*-benzyl alcohol, and *o*-hydroxymethylbenzoic acid lactone, were detected by mass spectrometry (MS) (Figure S4). Accordingly, the intermediate products of *o*-xylene photodegradation, such as *o*-benzoic acid, *o*-benzaldehyde, *o*-benzyl alcohol, and *o*-hydroxymethylbenzoic acid lactone, were strongly adsorbed on the surface of catalyst, occupying the active site on the surface of the catalyst, causing the catalyst to be deactivated.

Furthermore, the Er doping resulted in the formation of defect states (V_O) and increased the surface OH groups, in which V_O could adsorb more oxygen reacting with captured electrons ($V_O + O_2 \rightarrow$ absorbed oxygen (O_2^-, O_2^{2-}, O^-) + $e^- \rightarrow \bullet O_2^-$) and surface OH groups reacted with holes according to ($OH + h^+ \rightarrow \bullet OH$), further forming photoactive species ($\bullet O_2^-$ and •OH) to photodegrade gaseous VOCs. To this end, the effect of crystal defects (V_O) on photocatalytic activity in materials was still under debate. Theoretical calculations and experimental characterizations indicated that V_O affected the electronic structure,[59] charge transport, and surface adsorption for O_2 or H_2O of TiO_2.[60] Some authors[61] suggested that V_O would inhibit the recombination of photogenerated carriers, thus forming more active species conducive to the improvement of photocatalytic activity of the catalysts. However, other authors[49,62] hold the opposite opinion that the presence of V_O would serve as recombination centers, promoting the recombination of photogenerated carriers and then hindering the photocatalytic activity of materials. In our work, from the subsequent analysis, we could see that oxygen vacancies showed both the promotion and inhibition of the photocatalytic performance of the materials we had prepared. Therefore, from the removal efficiency of the catalyst with the most defects, it could be implied that a reasonable defect concentration could conduce the photocatalytic reaction process. According to previous reports,[63] when the body defect and the surface defect reached a certain ratio, the defect mainly appeared as a recombination center, decreasing the photocatalytic activity. Additionally, the formation of Er_2O_3 prevented the crystal grain growth of TiO_2, thereby increasing its specific surface area and improving the adsorption capacity of the as-prepared materials. Furthermore, the Er doping extended the light absorption characteristics of the samples in the visible and NIR region, which further improved the photocatalytic activity. Overall, it could be concluded that photocatalytic activity of the catalyst was associated with the synergistic effect of defects (V_O) and the intra-4f electronic structure of Er ion.

4. CONCLUSIONS

In summary, the Er-doped TiO_2 samples with various Er contents were synthesized and carried out the photocatalytic degradation of typical VOCs at a flow rate of 20 sccm. The results suggested that Er successfully occupied the Ti site in the crystal lattice, leading to the formation of oxygen vacancies (V_O) and Ti^{3+}, which significantly enhanced the photocatalytic performance of the catalyst. The incorporation of Er to TiO_2 delayed the deactivation of the catalyst during the degradation of *o*-xylene and promoted visible light ($\lambda > 420$ nm) activity to acetaldehyde, and the highest degradation efficiency was up to 25.5%. The presence of Er_2O_3 increased the specific surface area, hence increasing the adsorption capacity for VOCs. Moreover, $\bullet O_2^-$ played a more predominant role in the degradation of acetaldehyde and ethylene whereas •OH was the dominant active species for the degradation of *o*-xylene. Finally, the Er-doped catalyst exhibited excellent stability and high photocatalytic activity at a higher concentration and higher flow rate of VOCs. Subsequently, this work provided a stable and efficient photocatalyst, as well as guided significance for the design of catalysts and the selection of suitable catalysts for removing target VOCs in practical applications in the future.

■ ASSOCIATED CONTENT

Ⓢ Supporting Information

The Supporting Information is available free of charge on the ACS Publications website at DOI: 10.1021/acs.jpcc.9b02093.

> Supporting figures of XPS spectra and data for O 1s and Er 4d regions, degradation kinetics model of gas-phase VOCs and degradation rate constant, degradation efficiency of acetaldehyde under visible light ($\lambda > 420$ nm), degradation efficiency and rate constant of acetaldehyde at different flow rates, degradation rate constant of acetaldehyde at different concentrations, mass spectrometry of intermediates adsorbed on the surface of the catalyst during *o*-xylene degradation (PDF)

■ AUTHOR INFORMATION

Corresponding Authors

*E-mail: xxfshcn@163.com (X.X.).
*E-mail: jingsun@mail.sic.ac.cn (J.S.).

ORCID

Xiaofeng Xie: 0000-0003-1789-1084
Asad Mahmood: 0000-0002-5866-0680
Jing Sun: 0000-0003-1101-1584

Notes

The authors declare no competing financial interest.

■ ACKNOWLEDGMENTS

This work was financially supported by the National Key Research and Development Program of China (2016YFA0203000), the NSFC-DFG bilateral organization program (51761135107), the Youth Innovation Promotion Association CAS (2017042), the National Natural Science Foundation of China (41571130022), and Shanghai Sailing Program (18YF1426800).

■ REFERENCES

(1) Ng, N. L.; Kroll, J. H.; Chan, A. W. H.; Chhabra, P. S.; Flagan, R. C.; Seinfeld, J. H. Secondary Organic Aerosol Formation from M-Xylene, Toluene, and Benzene. *Atmos. Chem. Phys.* **2007**, *7*, 3909−3922.

(2) Huang, R. J.; Zhang, Y.; Bozzetti, C.; Ho, K. F.; Cao, J. J.; Han, Y.; Daellenbach, K. R.; Slowik, J. G.; Platt, S. M.; Canonaco, F.; et al. High Secondary Aerosol Contribution to Particulate Pollution During Haze Events in China. *Nature* **2014**, *514*, 218−222.

(3) Riipinen, I.; Yli-Juuti, T.; Pierce, J. R.; Petaja, T.; Worsnop, D. R.; Kulmala, M.; Donahue, N. M. The Contribution of Organics to Atmospheric Nanoparticle Growth. *Nat. Geosci.* **2012**, *5*, 453−458.

(4) Wang, S.; Ang, H. M.; Tade, M. O. Volatile Organic Compounds in Indoor Environment and Photocatalytic Oxidation: State of the Art. *Environ. Int.* **2007**, *33*, 694−705.

(5) Jeong, J.; Sekiguchi, K.; Lee, W.; Sakamoto, K. Photodegradation of Gaseous Volatile Organic Compounds (VOCs) Using TiO_2 Photoirradiated by an Ozone-Producing UV Lamp: Decomposition Characteristics, Identification of by-Products and Water-Soluble Organic Intermediates. *J. Photochem. Photobiol., A* **2005**, *169*, 279−287.

(6) Herrmann, J. M. Heterogeneous Photocatalysis: Fundamentals and Applications to the Removal of Various Types of Aqueous Pollutants. *Catal. Today* **1999**, *53*, 115−129.

(7) Akpan, U. G.; Hameed, B. H. Parameters Affecting the Photocatalytic Degradation of Dyes Using TiO_2-Based Photocatalysts: A Review. *J. Hazard. Mater.* **2009**, *170*, 520−529.

(8) Wang, M.; Ioccozia, J.; Sun, L.; Lin, C.; Lin, Z. Inorganic-Modified Semiconductor TiO_2 Nanotube Arrays for Photocatalysis. *Energy Environ. Sci.* **2014**, *7*, 2182−2202.

(9) Herrmann, J. M.; Tahiri, H.; AitIchou, Y.; Lassaletta, G.; GonzalezElipe, A. R.; Fernandez, A. Characterization and Photocatalytic Activity in Aqueous Medium of TiO_2 and Ag-TiO_2 Coatings on Quartz. *Appl. Catal., B* **1997**, *13*, 219−228.

(10) Fujishima, A.; Honda, K. Electrochemical Photolysis of Water at a Semiconductor Electrode. *Nature* **1972**, *238*, 37−38.

(11) Chen, X.; Shen, S.; Guo, L.; Mao, S. S. Semiconductor-Based Photocatalytic Hydrogen Generation. *Chem. Rev.* **2010**, *110*, 6503−6570.

(12) Huang, X.; Han, S.; Huang, W.; Liu, X. Enhancing Solar Cell Efficiency: The Search for Luminescent Materials as Spectral Converters. *Chem. Soc. Rev.* **2013**, *42*, 173−201.

(13) Zhou, J.; Liu, Q.; Feng, W.; Sun, Y.; Li, F. Upconversion Luminescent Materials: Advances and Applications. *Chem. Rev.* **2015**, *115*, 395−465.

(14) Jeon, S.; Braun, P. V. Hydrothermal Synthesis of Er-Doped Luminescent TiO_2 Nanoparticles. *Chem. Mater.* **2003**, *15*, 1256−1263.

(15) Frindell, K. L.; Bartl, M. H.; Robinson, M. R.; Bazan, G. C.; Popitsch, A.; Stucky, G. D. Visible and near-Ir Luminescence Via Energy Transfer in Rare Earth Doped Mesoporous Titania Thin Films with Nanocrystalline Walls. *J. Solid State Chem.* **2003**, *172*, 81−88.

(16) Shan, G.-B.; Demopoulos, G. P. Near-Infrared Sunlight Harvesting in Dye-Sensitized Solar Cells Via the Insertion of an Upconverter-TiO_2 Nanocomposite Layer. *Adv. Mater.* **2010**, *22*, 4373−4374.

(17) Xu, A. W.; Gao, Y.; Liu, H. Q. The Preparation, Characterization, and Their Photocatalytic Activities of Rare-Earth-Doped TiO_2 Nanoparticles. *J. Catal.* **2002**, *207*, 151−157.

(18) Liang, C.-H.; Hou, M.-F.; Zhou, S.-G.; Li, F.-B.; Liu, C.-S.; Liu, T. X.; Gao, Y. X.; Wang, X. G.; Lu, H. L. The Effect of Erbium on the Adsorption and Photodegradation of Orange I in Aqueous Er^{3+}-TiO_2 Suspension. *J. Hazard. Mater.* **2006**, *138*, 471−478.

(19) Wang, J.; Li, R.; Zhang, Z.; Sun, W.; Xu, R.; Xie, Y.; Xing, Z.; Zhang, X. Efficient Photocatalytic Degradation of Organic Dyes over Titanium Dioxide Coating Upconversion Luminescence Agent under Visible and Sunlight Irradiation. *Appl. Catal., A* **2008**, *334*, 227−233.

(20) Castañeda-Contreras, J.; Marañón-Ruiz, V. F.; Chiu-Zárate, R.; Pérez-Ladrón de Guevara, H.; Rodriguez, R.; Michel-Uribe, C. Photocatalytic Activity of Erbium-Doped TiO_2 Nanoparticles Immobilized in Macro-Porous Silica Films. *Mater. Res. Bull.* **2012**, *47*, 290−295.

(21) Hou, D.; Goei, R.; Wang, X.; Wang, P.; Lim, T. T. Preparation of Carbon-Sensitized and Fe-Er Codoped TiO_2 with Response Surface Methodology for Bisphenol a Photocatalytic Degradation under Visible-Light Irradiation. *Appl. Catal., B* **2012**, *126*, 121−133.

(22) Reszczynska, J.; Iwulska, A.; Sliwinski, G.; Zaleska, A. Characterization and Photocatalytic Activity of Rare Earth Metal-Doped Titanium Dioxide. *Physicochem. Probl. Miner. Process.* **2012**, *48*, 201−208.

(23) Verbruggen, S. W.; Masschaele, K.; Moortgat, E.; Korany, T. E.; Hauchecorne, B.; Martens, J. A.; Lenaerts, S. Factors Driving the Activity of Commercial Titanium Dioxide Powders Towards Gas Phase Photocatalytic Oxidation of Acetaldehyde. *Catal. Sci. Technol.* **2012**, *2*, 2311−2318.

(24) Dias, C. R.; Portela, M. F.; Bond, G. C. Oxidation of O-xylene to Phthalic Anhydride over V_2O_5/TiO_2 Catalysts.1. Influence of Catalyst Composition, Preparation Method and Operating Conditions on Conversion and Product Selectivities. *J. Catal.* **1995**, *157*, 344−352.

(25) Hauchecorne, B.; Tytgat, T.; Verbruggen, S. W.; Hauchecorne, D.; Terrens, D.; Smits, M.; Vinken, K.; Lenaerts, S. Photocatalytic Degradation of Ethylene: An Ftir in Situ Study under Atmospheric Conditions. *Appl. Catal., B* **2011**, *105*, 111−116.

(26) Yin, G.; Huang, X.; Chen, T.; Zhao, W.; Bi, Q.; Xu, J.; Han, Y.; Huang, F. Hydrogenated Blue Titania for Efficient Solar to Chemical Conversions: Preparation, Characterization, and Reaction Mechanism of CO_2 Reduction. *ACS Catal.* **2018**, *8*, 1009−1017.

(27) Li, W.; Frenkel, A. I.; Woicik, J. C.; Ni, C.; Shah, S. I. Dopant Location Identification in Nd^{3+}-Doped TiO_2 Nanoparticles. *Phys. Rev. B* **2005**, *72*, No. 155315.

(28) Reszczyńska, J.; Grzyb, T.; Wei, Z.; Klein, M.; Kowalska, E.; Ohtani, B.; Zaleska-Medynska, A. Photocatalytic Activity and Luminescence Properties of Re^{3+}-TiO_2 Nanocrystals Prepared by Sol-Gel and Hydrothermal Methods. *Appl. Catal., B* **2016**, *181*, 825−837.

(29) Meksi, M.; Turki, A.; Kochkar, H.; Bousselmi, L.; Guillard, C.; Berhault, G. The Role of Lanthanum in the Enhancement of Photocatalytic Properties of TiO_2 Nanomaterials Obtained by Calcination of Hydrogenotitanate Nanotubes. *Appl. Catal., B* **2016**, *181*, 651−660.

(30) Luo, W.; Li, R.; Liu, G.; Antonio, M. R.; Chen, X. Evidence of Trivalent Europium Incorporated in Anatase Tio2 Nanocrystals with Multiple Sites. *J. Phys. Chem. C* **2008**, *112*, 10370−10377.

(31) Reddy, B. M.; Chowdhury, B.; Smirniotis, P. G. An XPS Study of La_2O_3 and In_2O_3 Influence on the Physicochemical Properties of MoO_3/TiO_2 Catalysts. *Appl. Catal., A* **2001**, *219*, 53−60.

(32) Wang, G.; Qin, W.; Zhang, J.; Zhang, J.; Wang, Y.; Cao, C.; Wang, L.; Wei, G.; Zhu, P.; Kim, R. Enhancement of Violet and Ultraviolet Upconversion Emissions in Yb^{3+}/Er^{3+}-Codoped YF_3 Nanocrystals. *Opt. Mater.* **2008**, *31*, 296−299.

(33) Obregón, S.; Kubacka, A.; Fernández-García, M.; Colón, G. High-Performance Er^{3+}-TiO_2 System: Dual up-Conversion and Electronic Role of the Lanthanide. *J. Catal.* **2013**, *299*, 298−306.

(34) Bhethanabotla, V. C.; Russell, D. R.; Kuhn, J. N. Assessment of Mechanisms for Enhanced Performance of Yb/Er/Titania Photocatalysts for Organic Degradation: Role of Rare Earth Elements in the Titania Phase. *Appl. Catal., B* **2017**, *202*, 156−164.

DOI: 10.1021/acs.jpcc.9b02093
J. Phys. Chem. C 2019, 123, 12321−12334

(35) Salari, M.; Konstantinov, K.; Liu, H. K. Enhancement of the Capacitance in TiO_2 Nanotubes through Controlled Introduction of Oxygen Vacancies. *J. Mater. Chem.* **2011**, *21*, 5128−5133.

(36) Anpo, M.; Che, M.; Fubini, B.; Garrone, E.; Giamello, E.; Paganini, M. C. Generation of Superoxide Ions at Oxide Surfaces. *Top. Catal.* **1999**, *8*, 189−198.

(37) Zuo, F.; Wang, L.; Wu, T.; Zhang, Z.; Borchardt, D.; Feng, P. Self-Doped Ti^{3+} Enhanced Photocatalyst for Hydrogen Production under Visible Light. *J. Am. Chem. Soc.* **2010**, *132*, 11856−11857.

(38) Górska, P.; Zaleska, A.; Kowalska, E.; Klimczuk, T.; Sobczak, J. W.; Skwarek, E.; Janusz, W.; Hupka, J. TiO_2 Photoactivity in Vis and UV Light: The Influence of Calcination Temperature and Surface Properties. *Appl. Catal., B* **2008**, *84*, 440−447.

(39) Eom, J. Y.; Lim, S. J.; Lee, S. M.; Ryu, W. H.; Kwon, H. S. Black Titanium Oxide Nanoarray Electrodes for High Rate Li-Ion Microbatteries. *J. Mater. Chem. A* **2015**, *3*, 11183−11188.

(40) Rjeb, A.; Letarte, S.; Tajounte, L.; El Idrissi, M. C.; Adnot, A.; Roy, D.; Claire, Y.; Kaloustian, J. Polypropylene Natural Aging Studied by X-Ray Photoelectron Spectroscopy. *J. Electron Spectrosc. Relat. Phenom.* **2000**, *107*, 221−230.

(41) Lettmann, C.; Hildenbrand, K.; Kisch, H.; Macyk, W.; Maier, W. F. Visible Light Photodegradation of 4-Chlorophenol with a Coke-Containing Titanium Dioxide Photocatalyst. *Appl. Catal., B* **2001**, *32*, 215−227.

(42) Wang, Y.; Cai, J.; Wu, M.; Zhang, H.; Meng, M.; Tian, Y.; Ding, T.; Gong, J.; Jiang, Z.; Li, X. Hydrogenated Cagelike Titania Hollow Spherical Photocatalysts for Hydrogen Evolution under Simulated Solar Light Irradiation. *ACS Appl. Mater. Interfaces* **2016**, *8*, 23006−23014.

(43) Chen, X.; Liu, L.; Yu, P. Y.; Mao, S. S. Increasing Solar Absorption for Photocatalysis with Black Hydrogenated Titanium Dioxide Nanocrystals. *Science* **2011**, *331*, 746−750.

(44) Ardizzone, S.; Bianchi, C. L.; Cappelletti, G.; Gialanella, S.; Pirola, C.; Ragaini, V. Tailored Anatase/Brookite Nanocrystalline TiO_2. The Optimal Particle Features for Liquid- and Gas-Phase Photocatalytic Reactions. *J. Phys. Chem. C* **2007**, *111*, 13222−13231.

(45) Swami, G. T. K.; Stageberg, F. E.; Goldman, A. M. XPS Characterization of Erbium Sesquioxide and Erbium Hydroxide. *J. Vac. Sci. Technol., A* **1984**, *2*, 767−770.

(46) Mamaghani, A. H.; Haghighat, F.; Lee, C. S. Gas Phase Adsorption of Volatile Organic Compounds onto Titanium Dioxide Photocatalysts. *Chem. Eng. J.* **2018**, *337*, 60−73.

(47) Wei, Z.; Liu, Y.; Wang, J.; Zong, R.; Yao, W.; Wang, J.; Zhu, Y. Controlled Synthesis of a Highly Dispersed Bipo4 Photocatalyst with Surface Oxygen Vacancies. *Nanoscale* **2015**, *7*, 13943−13950.

(48) Reszczyńska, J.; Grzyb, T.; Sobczak, J. W.; Lisowski, W.; Gazda, M.; Ohtani, B.; Zaleska, A. Visible Light Activity of Rare Earth Metal Doped (Er^{3+}, Yb^{3+} or Er^{3+}/Yb^{3+}) Titania Photocatalysts. *Appl. Catal., B* **2015**, *163*, 40−49.

(49) Wang, J.; Tafen, D. N.; Lewis, J. P.; Hong, Z.; Manivannan, A.; Zhi, M.; Li, M.; Wu, N. Origin of Photocatalytic Activity of Nitrogen-Doped TiO_2 Nanobelts. *J. Am. Chem. Soc.* **2009**, *131*, 12290−12297.

(50) Zhang, Z.; Xu, M.; Ho, W.; Zhang, X.; Yang, Z.; Wang, X. Simultaneous Excitation of $PdCl_2$ Hybrid Mesoporous g-C_3N_4 Molecular/Solid-State Photocatalysts for Enhancing the Visible-Light-Induced Oxidative Removal of Nitrogen Oxides. *Appl. Catal., B* **2016**, *184*, 174−181.

(51) Coronado, J. M.; Maira, A. J.; Conesa, J. C.; Yeung, K. L.; Augugliaro, V.; Soria, J. Epr Study of the Surface Characteristics of Nanostructured TiO_2 under UV Irradiation. *Langmuir* **2001**, *17*, 5368−5374.

(52) Zhang, Z.; Chen, P.; Murakami, T. N.; Zakeeruddin, S. M.; Graetzel, M. The 2,2,6,6-Tetramethyl-1-Piperidinyloxy Radical: An Efficient, Iodine-Free Redox Mediator for Dye-Sensitized Solar Cells. *Adv. Funct. Mater.* **2008**, *18*, 341−346.

(53) Ding, X.; Ho, W.; Shang, J.; Zhang, L. Self Doping Promoted Photocatalytic Removal of No under Visible Light with Bi2moo6: Indispensable Role of Superoxide Ions. *Appl. Catal., B* **2016**, *182*, 316−325.

(54) Chen, P.; Wang, F.; Chen, Z. F.; Zhang, Q.; Su, Y.; Shen, L.; Yao, K.; Liu, Y.; Cai, Z.; Lv, W.; et al. Study on the Photocatalytic Mechanism and Detoxicity of Gemfibrozil by a Sunlight-Driven TiO_2/Carbon Dots Photocatalyst: The Significant Roles of Reactive Oxygen Species. *Appl. Catal., B* **2017**, *204*, 250−259.

(55) Zheng, W.; Huang, P.; Tu, D.; Ma, E.; Zhu, H.; Chen, X. Lanthanide-Doped Upconversion Nano-Bioprobes: Electronic Structures, Optical Properties, and Biodetection. *Chem. Soc. Rev.* **2015**, *44*, 1379−1415.

(56) Ameen, M. M.; Raupp, G. B. Reversible Catalyst Deactivation in the Photocatalytic Oxidation of Dilute O-xylene in Air. *J. Catal.* **1999**, *184*, 112−122.

(57) Augugliaro, V.; Coluccia, S.; Loddo, V.; Marchese, L.; Martra, G.; Palmisano, L.; Schiavello, M. Photocatalytic Oxidation of Gaseous Toluene on Anatase TiO_2 Catalyst: Mechanistic Aspects and Ft-Ir Investigation. *Appl. Catal., B* **1999**, *20*, 15−27.

(58) Einaga, H.; Futamura, S.; Ibusuki, T. Heterogeneous Photocatalytic Oxidation of Benzene, Toluene, Cyclohexene and Cyclohexane in Humidified Air: Comparison of Decomposition Behavior on Photoirradiated TiO_2 Catalyst. *Appl. Catal., B* **2002**, *38*, 215−225.

(59) Bilmes, S. A.; Mandelbaum, P.; Alvarez, F.; Victoria, N. M. Surface and Electronic Structure of Titanium Dioxide Photocatalysts. *J. Phys. Chem. B* **2000**, *104*, 9851−9858.

(60) Schaub, R.; Thostrup, P.; Lopez, N.; Laegsgaard, E.; Stensgaard, I.; Norskov, J. K.; Besenbacher, F. Oxygen Vacancies as Active Sites for Water Dissociation on Rutile TiO_2 (110). *Phys. Rev. Lett.* **2001**, *87*, 4.

(61) Wang, G. M.; Wang, H. Y.; Ling, Y. C.; Tang, Y. C.; Yang, X. Y.; Fitzmorris, R. C.; Wang, C. C.; Zhang, J. Z.; Li, Y. Hydrogen-Treated TiO_2 Nanowire Arrays for Photoelectrochemical Water Splitting. *Nano Lett.* **2011**, *11*, 3026−3033.

(62) Pan, X.; Zhang, N.; Fu, X.; Xu, Y. J. Selective Oxidation of Benzyl Alcohol over TiO_2 Nanosheets with Exposed {001} Facets: Catalyst Deactivation and Regeneration. *Appl. Catal., A* **2013**, *453*, 181−187.

(63) Kong, M.; Li, Y.; Chen, X.; Tian, T.; Fang, P.; Zheng, F.; Zhao, X. Tuning the Relative Concentration Ratio of Bulk Defects to Surface Defects in TiO_2 Nanocrystals Leads to High Photocatalytic Efficiency. *J. Am. Chem. Soc.* **2011**, *133*, 16414−16417.